Article:
Knox, CS orcid.org/0000-0002-4673-5649, Vaughan, MT orcid.org/0000-0002-8336-2183, Burnett, AD orcid.org/0000-0003-2175-1893 et al. (5 more authors) (2022) Effects of structural ordering on infrared active vibrations within $Bi_2(Te_{(1-x)}Se_x)_3$. Physical Review B, 106 (24). 245203. ISSN 2469-9950

https://doi.org/10.1103/physrevb.106.245203

Effects of Structural Ordering on IR Active Vibrations Within $\mathbf{Bi_2(Te_{(1-x)}Se_x)_3}$

Craig S. Knox [1,2], Matthew T. Vaughan [1], Andrew D. Burnett [1], Mannan Ali [2], Satoshi Sasaki [2], Edmund H. Linfield [1], Alexander Giles Davies [1], and Joshua R. Freeman [1]

[1] *School of Electronic and Electrical Engineering, University of Leeds, Leeds LS2 9JT, United Kingdom*

[2] *School of Physics and Astronomy, University of Leeds, Leeds LS2 9JT, United Kingdom*

(Dated: 2022-12-13)

Abstract

We have performed a materials investigation into the properties of the THz conductivity spectra in the ternary alloy $Bi_2(Te_{(1-x)}Se_x)_3$ as a function of selenium fraction, x and temperature. We find that the reduction in crystalline anharmonicity caused by the preferential ordering of the $x = 1/3$ phase of $Bi_2(Te_{(1-x)}Se_x)_3$ results in the prominent E_u^1 phonon (occurring between 1.5 and 1.9 THz) red-shifting on cooling less than the binary Bi_2Te_3 and Bi_2Se_3 samples. We also find that the E_u^1 phonon couples to an electronic continuum at low temperatures ($T \leqslant 40\,K$), regardless of $Bi_2(Te_{(1-x)}Se_x)_3$ stoichiometry or the Hall mobility of the topological insulator crystal. These results highlight the role that these optical modes play in the electronic and thermal transport within this ternary alloy, and pave the way for exploring the interesting phonon dynamics within these topological insulator and thermoelectric materials.

I. INTRODUCTION

Topological insulators are a class of materials where the bulk band-gap is bridged by conducting, spin filtered surface states, which are protected from elastic backscattering by the symmetry of the electronic bands [1]. Bismuth selenide (Bi_2Se_3), bismuth telluride (Bi_2Te_3) and their ternary alloy ($Bi_2(Te_{(1-x)}Se_x)_3$) are strong 3D topological insulators with large bulk bandgaps [2, 3], in addition to being efficient room temperature thermoelectrics [4, 5]. These topological insulators host a single set of metallic surface states at the Γ point, which makes exploration of the optical properties an attractive prospect, especially as plasmonic modes that carry pure spin currents have been predicted to arise within these topological insulators [6].

Topological protection of the surface states does not extend to inelastic scattering, such as electron-phonon interactions [7], this becomes especially important when we consider the E_u^1 phonon occurring between 1.5 and 1.9 THz in Bi_2Te_3 and Bi_2Se_3, respectively. The electron-phonon interaction between this optical mode and the surface states has been predicted to be particularly strong [8], which when combined with the Dresselhaus spin-orbit coupling arising from the crystal structure, can alter the spin texture of the surface states [7]. In addition, this phonon mode has a very pronounced effect on the dielectric function [9–11], leading to extreme anisotropy within the permittivity and an indefinite permittivity tensor, making both Bi_2Te_3 and Bi_2Se_3 hyperbolic media in the terahertz frequency regime

[12, 13].

The crystal structure of these topological insulators is composed of chemically bonded quintuple layers, bonded to each other by weak van der Waals forces. These quintuple layers order in the sequence; C_1–Bi–C_2–Bi–C_1, where C_n can be occupied by Te or Se in Bi_2Te_3 and Bi_2Se_3 respectively. However Se is more electronegative than Te, and therefore, as we incorporate Se into Bi_2Te_3 to form the ternary alloy $Bi_2(Te_{(1-x)}Se_x)_3$, Se preferentially lies on the C_2 sites [14] as the Bi-Se bond is favoured over the Bi-Te bond [15], and the C_2 sites form two Bi–C_2 bonds. This makes the $Bi_2(Te_{(1-x)}Se_x)_3$ system an extremely interesting topic of study, as this preferential order should minimise the formation of the vacancy defects common in Bi_2Se_3 and the Te-Bi antisite defects common in Bi_2Te_3 [16]. This becomes especially important when considering the thermoelectric properties osf Bi_2Te_3 and Bi_2Se_3, as manipulating the number of defects is essential to minimise the lattice thermal conductivity, increasing the thermoelectric figure of merit [5]. In addition to controlling the density of defects, since as-grown Bi_2Se_3 is n-type, and Bi_2Te_3 may be grown p-type under the correct conditions, tuning the stoichiometry of $Bi_2(Te_{(1-x)}Se_x)_3$ can be used in order to access a mid-gap, surface dominated state [2]. Previous studies have noted that the preferential ordering of the $x = 1/3$ phase of $Bi_2(Te_{(1-x)}Se_x)_3$ has a pronounced effect on the Raman active vibrational modes of $Bi_2(Te_{(1-x)}Se_x)_3$[9, 14]. However, the commonly observed Raman modes (E_g^1, A_{1g}^1, E_g^2 and A_{1g}^2) vibrate around the C_2 sites as a centre of mass, and so are less sensitive to the occupation of that site, whereas the IR-active E_u^1 mode does not share this centre of mass [9].

The temperature dependence of the Raman active modes within $Bi_2(Te_{(1-x)}Se_x)_3$ can be described by the anharmonic decay of optical phonons. In a general sense, this anharmonic process is characterised by the decay of one or more optical phonons into two or more acoustic phonons [17]. As optical phonons do not contribute significantly to the thermal conductivity of a bulk material due to their small mean free path, this anharmonic scattering is an important contributor to the lattice thermal conductivity [18]. However, optical phonons can make a significant contribution to the lattice thermal conductivity in nanostructures due to the boundary scattering of acoustic phonons [19]. This makes the study of the temperature dependent phonon dynamics within the $Bi_2(Te_{(1-x)}Se_x)_3$ material system an interesting topic of study, as the phonon lifetime as a function of x and its temperature evolution (and thus the degree of anharmonic scattering) can be used to select materials

and device dimensions for thermoelectric applications.

In this work, we present a detailed material study of $Bi_2(Te_{(1-x)}Se_x)_3$ films with varying Se content, grown by molecular beam epitaxy. We explore the effect that changing the Se content has on the optical properties through temperature dependent THz time-domain spectroscopy (THz-TDS), and find that structural anharmonicity plays a key role in determining the temperature dependence of the E_u^1 phonon, which we support with solid-state density functional theory calculations. We also observe that in all the samples studied here, the E_u^1 phonon appears to couple to an electronic continuum at low temperatures, highlighting the electron-phonon coupling within this topological insulator system.

II. EXPERIMENTAL SECTION

The samples were prepared within a solid-source MBE system, with a base pressure of $\approx 1 \times 10^{-10}$ Torr. The samples were grown on [0001] oriented Al_2O_3 substrates by co-deposition of evaporated bismuth, selenium and tellurium. The bismuth and selenium were evaporated from dual-filament Knudsen cells, whereas the tellurium was evaporated from a valved cracker source. The samples were grown at substrate temperatures of $230 - 240$ °C, measured by a thermocouple attached to the sample manipulator.

All the samples were grown under chalcogenide rich conditions, such that the total chalchogenide flux is at least 20 times that of the bismuth flux. This is essential in order to minimise the formation of chalcogenide vacancies [20], ensure the correct phase of topological insulator is grown [21], and to ensure that the growth rate is determined solely by the bismuth flux [14]. The ratio of tellurium and selenium fluxes was then tuned in order to select the desired stoichiometry of $Bi_2(Te_{(1-x)}Se_x)_3$. The crystallographic properties of $Bi_2(Te_{(1-x)}Se_x)_3$ samples were subsequently analysed by x-ray reflectivity and x-ray diffraction, using Cu K_α radiation, before being diced for DC transport measurements and substrate-referenced THz-TDS. For transport measurements the samples were contacted using silver paint, in a van der Pauw configuration, before being loaded into a continuous flow He cryostat with a base temperature of 1.6 K and an 8 T superconducting magnet. Transverse and Hall conductivities were then measured using standard lockin techniques with a source-drain bias current of 1 μA at a frequency of 119.77 Hz.

The THz-TDS measurements were undertaken between 3 and 300 K in a continuous flow

He cryostat. Both quartz and transparent polymethylepentene (TPX) windows were used in this study, with negligible effects on the observed spectra, aside from a weak resonance at ≈ 4 THz from the quartz windows. The TPX windows do not show this resonance. The sample to be measured, along with a bare sapphire reference, were then mounted co-axially on the cold finger of the cryostat, which was subsequently evacuated and cooled to the required temperature. The time-domain signal was then acquired using 20 fs pulses from a Ti-Sapphire laser, a delay stage and two LT-GaAs-on quartz photo-conductive antennas, with a spectral range of $0.5 - 4.5$ THz. Further details can be found in Ref. [22]. The transmission through the sample was measured at normal incidence; a typical set of electric-field pulses are shown in figure 1.

The time-domain data is then trimmed (with a boxcar window) to remove unwanted Fabry-Perot reflections and zero-padded by 5 ps in either direction before a Fourier transform was taken. The complex transmittance of the topological insulator is then defined as $T(\omega) = \frac{E_{\text{sample}}(\omega)}{E_{\text{reference}}(\omega)}$ where $E(\omega)$ is the complex result of the Fourier transform. From the complex transmittance, the optical conductivity can then be determined via [23];

$$\tilde{\sigma}(\omega) = \left(\frac{1}{T(\omega)} - 1\right) \frac{1 + n_{\text{reference}}}{Z_0 d} \tag{1}$$

where Z_0 is the impedance of free space, d is the thickness of the topological insulator film and $n_{\text{reference}}$ is the refractive index of the substrate, as determined from the sapphire reference measurement.

III. RESULTS

The $(\omega - 2\theta)$ XRD scans for the $Bi_2(Te_{(1-x)}Se_x)_3$ composition range studied here is shown in figure 2a. All samples show well ordered $[000l]$ peaks, showing that the c-axis of the TI is oriented parallel to the growth direction. As the Se flux is increased, the $[000, 15]$ peak shifts to higher diffraction angles, indicating a smaller c-axis lattice constant, as shown in figure 2b. Vegard's law is then used to determine the nominal selenium content of the topological insulator alloy (shown in the inset of 2b) [16, 24]. We find that, even with a very large Se/Te flux ratio, that the $x = 0.33$ phase is favoured, and we were unable to produce $Bi_2(Te_{(1-x)}Se_x)_3$ with $0 < x \leqslant 0.33$.

The behaviour of the [000,12] peak is somewhat more interesting. In Bi_2Te_3, this peak is

extremely weak, to the point that it is indistinguishable from the background. However, as more Se is incorporated into the alloy, the intensity of this peak rises, reaching a maximum when $x = 0.35$, as shown in figure 2c, where the amplitude of a gaussian fitted to the $[000, 12]$ peak is plotted as a function of nominal selenium content. The intensity then decreases, until the peak vanishes at $x = 0.84$. Finally, as x approaches 1, the peak reappears. This is evidence of the preferential ordering of the topological insulator alloy, where the Se occupies the central plane of the quintuple layer [14]. We note that the FHWM of the $[000, 15]$ peak (shown in the inset of figure 2c), associated with crystalline disorder, is significantly higher for the $x = 0.48, 0.52, 57$ and 0.84 samples. This may be indicative of the random location of Se atoms on the C_1 sites on the outside of the quintuple layer.

The low-frequency electrical properties of the films were subsequently analysed through electrical transport measurements. On cooling, all $Bi_2(Te_{(1-x)}Se_x)_3$ samples show sheet resistances that decrease with decreasing temperature before saturating at a low temperature, as shown in figure 3a. This metallic behaviour implies that the conduction through these topological insulator samples is dominated by the trivial bulk carriers, regardless of the Se content. This observation is confirmed when we consider the Hall resistance of these samples at low temperature (1.8 K). All samples show n-type, electron-dominated transport, including the $x = 0$ Bi_2Te_3 sample, which does prevent us from using the stoichiometry of $Bi_2(Te_{(1-x)}Se_x)_3$ to probe the mid-gap, surface dominated state. Bi_2Te_3 grown by MBE is often n-type, possibly due to the large excess of Te used to prevent the formation of vacancy defects [25, 26]. Most samples show a strong non-linearity in the Hall resistance (shown for Bi_2Se_3 in figure 3b) at 1.8 K. This is indicative of the presence of two different carrier species with different mobilities [27, 28], possibly indicating the co-existence of bulk and surface states. We therefore fit the Hall trace to a two-band model [28], the results of which are shown in table I. It is worth noting that the $x = 0.48$ and $x = 0.52$ samples, with the lowest overall mobility, do not show two-carrier transport. It is likely that a large number of intrinsic defects results in Fermi-level pinning within the bulk bands, which obscures the surface state transport.

For the samples which do show two-carrier transport, band 1 shows a large number ($\approx \times 10^{14}$ cm^{-2}) of low mobility carriers, whereas band 2 shows a much smaller number of higher mobility carriers. In fact, band 2 consistently shows carrier densities between $3 - 30 \times 10^{12}$ cm^{-2}, which is similar to the carrier densities observed for topological surface

states in other studies [20, 29].

We move on to consider the optical properties of these topological insulators. The THz conductivity spectra (shown for Bi_2Te_3 and Bi_2Se_3 in figure 4) are largely dominated by the prominent E_u^1 phonon [9, 10] that occurs close to 1.5 and 2 THz in Bi_2Te_3 and Bi_2Se_3, respectively. It is worth noting that we do not observe the E_u^2 phonon between $\approx 3{-}4$ THz [9–11] in any of our samples at any temperature. As the E_u^2 phonon polariton is extremely weak when compared to the E_u^1 polariton [9, 30], we reason that the large conductivity response, combined with the lower signal to noise at this higher frequency mask this vibrational mode.

The spectra can be described by a modified Drude-Lorenz fit to the conductivity including a Drude term (described by σ_{DC}, the DC conductivity, and τ, the Drude scattering time), a single Lorentzian oscillator for the E_u^1 phonon (described by $A_{E_u^1}$, the amplitude of the E_u^1 phonon; $\Omega_{E_u^1}$ the frequency of the E_u^1 phonon; and $\gamma_{E_u^1}$ the scattering frequency of the E_u^1 phonon, proportional to the phonon linewidth), and a high frequency term, ϵ_∞, to account for higher-energy excitations on the THz conductivity spectrum [31, 32].

$$\tilde{\sigma}(\omega) = \frac{-\sigma_{DC}}{i\omega\tau - 1} - \frac{i\epsilon_0\omega A_{E_u^1}^2}{\Omega_{E_u^1}^2 - \omega^2 - (i\omega\gamma_{E_u^1})} - (\epsilon_\infty - 1)i\omega\epsilon_0 \tag{2}$$

THz scans at a range of temperatures were then performed for all samples shown in figure 2, with the results summarised in figure 5, which we will now go on to discuss in detail. There is a continuous variation in the E_u^1 phonon frequency as the Se content is increased, as shown in figure 5a, however, unlike the commonly observed A_g^1 Raman active mode [9, 14, 33], the largest frequency change occurs between $0 \leqslant x \leqslant 1/3$. This is a consequence of the preferential ordering within the $Bi_2(Te_{(1-x)}Se_x)_3$ alloys. The E_u^1 phonon, shown schematically in the inset of 4c, involves a vibration of the central atom within the quintuple layer (C_2 in the inset of 4c), unlike the Raman active modes, which all vibrate around this site [9, 34]. As such, the IR active E_u^1 mode is far more sensitive to the occupation of that C_2 site, which we have already established is preferentially occupied by Se in the $0 \leqslant x \leqslant 1/3$ regime.

On cooling, the conductivity of the $Bi_2(Te_{(1-x)}Se_x)_3$ samples, obtained from fitting the complex conductivity spectra, increases (as shown in figure 5b). This agrees with figure 3a, implying that the bulk carriers make a significant contribution to both the Drude background seen in the THz conductivity spectra and the DC transport [30]. It is worth noting that

the conductivities fitted from the THz spectra are consistently lower than the conductivities extracted from the transport measurements. Such a trend is consistently observed in THz and mid-IR measurements of highly conductive samples [35, 36], and could arise due to the DC conductivity being weighted towards high-angle scattering events, whereas the THz transmission is sensitive to all scattering events [37].

As shown in figure 4, as the topological insulator sample is cooled, the E_u^1 mode gets significantly sharper, and the phonon frequency red-shifts. The trend in phonon frequency, for the Bi_2Se_3 sample, is outlined in the inset of figure 5a whereas the trend in the phonon scattering frequency is shown for all samples in figure 5c. We note that in both the phonon frequency and the scattering parameter, there seems to be two distinct regimes; a high temperature regime where the phonon red-shifts and narrows in an almost linear fashion, and a low temperature regime ($T \leqslant 50$ K) dominated by a sharp increase and gradual decay of the phonon width and frequency.

The red-shift on cooling observed in the phonon frequency is a commonly observed feature of this E_u^1 mode [9–11], in contrast with the E_u^2 mode and every commonly observed Raman mode, which all blue-shift on cooling at a rate similar to that we observe for the E_u^1 phonon [9, 38, 39]. We summarise the temperature dependence of the E_u^1 phonon mode in the high temperature regime in figure 5d by plotting the rate of change of $\Omega_{E_u^1}$ and $\gamma_{E_u^1}$ with temperature. In these materials, within this high temperature regime, the phonon dynamics are influenced by anharmonic phonon scattering [40]. Both the third order (cubic) and fourth order (quartic) anharmonic terms contribute to the phonon dynamics, but crucially the quartic anharmonicity term, to first order in the perturbation theory, only contributes to the phonon frequency shift. By contrast, the cubic term (to second order in the perturbation theory) contributes to both the thermal broadening of the phonon mode and the temperature dependent shift in the phonon frequency. We can gain some insight into the relative contribution of each by noting that the temperature dependent shift in the phonon frequency induced by the cubic and quartic anharmonicity terms are of opposite signs, with a cubic anharmonicity inducing a blue-shift on cooling and a quartic anharmonicity inducing a red shift on cooling [41–43].

We note that the red-shift on cooling and the thermal narrowing of the E_u^1 mode is smallest for the $x = 0.33$ and 0.35 samples. Additionally, at 290 K, the $x = 0.33$ sample has the smallest phonon scattering parameter, as shown in figure 5c. Finally we note that

the trend in phonon properties tracks with the trend in the amplitude of the $[000, 12]$ peak, shown in figure 2c. In order to determine the origin of this trend, we used density functional theory to understand the phonon properties of materials. Calculations were performed using VASP [44] the Perdew-Burke-Ernzerhof (PBE) functional [45], with the D3-BJ [46, 47] dispersion correction and the Projector Augmented Wave (PAW) pseudo-potentials [48] distributed with VASP 5.4.1. A plane-wave cutoff of 520 eV was used and the wavefunction was converged so that the energy changed by less than 1×10^{-4} eV with both the atom positions and unit cell dimensions optimised. Calculations were performed using a $1 \times 1 \times 1$ conventional cell with a Monkhorst-Pack [49] grid of $9 \times 9 \times 1$. Initial structures of Bi_2Se_3, Bi_2Te_3 and Bi_2Te_2Se (where all C_2 sites are occupied with Se and all C_1 sites are occupied with Te) with $R\bar{3}m$ space group symmetry were taken from the Materials Project [50]. After structural optimisation, harmonic phonon frequencies were calculated using the Phonopy [51] python code with VASP as the force calculator. Phonon frequencies of other compositions of $Bi_2(Te_{(1-x)}Se_x)_3$ were not calculated as both the preferential ordering and non-integer fractioning lead to a reduction in crystal symmetry and ambiguity in the actual structure being measured, requiring the study of a large number of possible supercells which is beyond the scope of this work.

To understand the anharmonic temperature shifts of the E_u^1 and A_{1g}^1 phonons using these calculations we then followed the approach used by Skelton et.al. [52]. Here we begin by mapping out the 1D potential-energy surface of the phonon mode eigenvector in each of the three materials. The potential energy along the mode as a function of the normal-mode coordinate, Q, can then be fitted to a 6-power polynomial with the potential energy surfaces of these three structures for the E_u^1 phonon shown in figure 6a. 1D Schrödinger equations for each of these potentials can then be solved with the eigenvalues generated used to determine an anharmonic vibrational partition function. This, in turn, allows an effective renormalized harmonic frequency for the E_u^1 mode at a specific temperature to be determined. It is worth noting that this model does not account for electron-phonon coupling, spin-orbit coupling or thermal expansion effects, which play an important role in the temperature dependent phonon dynamics of these materials [17, 42].

When we perform these calculations on the A_{1g}^1 mode, we find that the phonon frequency does not change significantly as a function of temperature. It is important to note that the A_{1g}^1 mode vibrates around the C_2 sites as a centre of mass. This, combined with the

fact that our calculations do not account for thermal expansion effects may explain the discrepancy between our calculations and the observed blue-shift on cooling [9, 17]. When we consider the IR-active E_u^1 phonon, we find a significant red-shift on cooling, that is significantly smaller in Bi_2Te_2Se when compared to Bi_2Te_3 and Bi_2Se_3 (shown in figure 6b), which agrees with our experimental observations. This leads us to two conclusions; firstly, the observed red shift of the phonon frequency on cooling implies that the quartic anharmonicity plays a larger role in the temperature dependent dynamics of the E_u^1 mode for all x in $Bi_2(Te_{(1-x)}Se_x)_3$ when compared to the Raman active modes. Secondly, the fact that the properties of the E_u^1 phonon within the $x = 1/3$ phase of $Bi_2(Te_{(1-x)}Se_x)_3$ show the smallest response to changes in temperature arises from the interaction between the preferential ordering of that phase and the anharmonic phonon scattering. This may arise due to the preferential ordering disrupting the long range interactions that can propogate through the crystal structures of binary Bi_2Te_3 and Bi_2Se_3[18].

At the molecular level, these long-range interactions can be understood by considering the p-orbitals, which play a dominant role in the bonding within Bi_2Te_3 and Bi_2Se_3. Due to the shape of these p-orbitals, any perturbation of an atom by a phonon will result in electrons on an adjacent atom moving to the opposite side of their host atom. As the p-orbitals within these materials form long chains of co-linear bonds [53] within a rock-salt like structure, this perturbation can propagate for large distances (up to 0.9 nm [18]), resulting in an anharmonic crystalline potential. Due to Se preferentially lying on the C_2 sites within the quintuple layer, as x in $Bi_2(Te_{(1-x)}Se_x)_3$ approaches 1/3, the crystal structure will be warped as the Bi–Se bonds are shorter than similar Bi–Te bonds [54, 55]. This distortion away from the rock salt-like structure will disrupt the long-range interactions that exists within Bi_2Te_3, as the bonds within the quintuple layer will no longer be equivalent, inhibiting the propagation of the electronic perturbation, resulting in a smaller anharmonic temperature-dependent frequency shift [18]. As x in $Bi_2(Te_{(1-x)}Se_x)_3$ increases past 1/3, and the C_1 sites start being populated with Se, the chains of equivalent p-orbitals start being re-formed (now with Se–Bi–Se bonds, rather than Te–Bi–Te bonds) and the anharmonic frequency shift rises.

It is important to note that the experimental rate at which the phonon red-shifts on cooling never returns to the value seen in pure Bi_2Te_3, which runs counter to our simulations, which predict that Bi_2Se_3 should have the largest anharmonic temperature dependent frequency shift, as shown in figure 6b. This may be due to the interplay of the electron-

phonon coupling of this E_u^1 mode and the defects within the $Bi_2(Te_{(1-x)}Se_x)_3$ sample. The electron-phonon interaction opens new decay paths for optical phonons [56] however, those decay mechanisms and their temperature dependence can be influnced by the scattering rate of electrons, and therefore the density of defects [57]. It is possible that the variation in the strength of the electron-phonon coupling with x in $Bi_2(Te_{(1-x)}Se_x)_3$[2, 8] could account for this discrepancy. Further *ab initio* calculations, accounting for electron-phonon and spin-orbit interactions, should shed light on how the temperature dependent phonon dynamics evolve over a wider range of alloy compositions, and could reveal how the phonon dynamics studied here impact the thermoelectric figure of merit.

Finally, we consider the low temperature regime where both the phonon frequency and the phonon scattering parameter increases below 50 K, accompanied by a drop in the fitted conductivity (as shown in 5b). Importantly, the temperature at which the sudden rise of the phonon parameters occurs seems to be largely independent of x, with the maximum phonon linewidth occurring between $20 - 30$ K. This implies that this feature is not due to phonon freeze-out, which should be strongly dependent on the Se content [58, 59]. A change in the phonon frequency, along with an increase in the phonon linewidth is a possible indicator of coupling between the phonon mode and some external continuum [17, 60]. Due to the concurrent drop in the fitted THz conductivity and the lack of isoenergetic vibrational modes at these temperatures [61] (the Raman active A_g^1 mode is similar in energy at room temperature, but blue-shifts on cooling [8, 9, 17]) we infer that the E_u^1 phonon is coupling to an electronic continuum, rather than a vibrational one.

While the E_u^1 mode has been predicted to couple strongly to the surface states within Bi_2Se_3 and Bi_2Te_3 [8], it is unclear if the coupling we observe here is due to electron phonon coupling to surface states. We note that only one carrier species is observed in transport measurements of the $x = 0.48$ and $x = 0.52$ samples (as shown in table I), and yet these samples also show the increase in phonon linewidth. This implies that, while the E_u^1 phonon may couple to the surface states, it may also couple with bulk or impurity bands.

IV. CONCLUSIONS

We have grown a series of $Bi_2(Te_{(1-x)}Se_x)_3$ samples with varying Te/Se flux ratios by MBE. The crystal quality was analysed by X-ray diffraction measurements and the selenium

content of the alloy samples was extracted via Vegard's law. The properties of the E_u^1 mode and the optical conductivities were then analysed as a function of temperature by THz-TDS. We find that the trend in the Drude conductivity agrees with the trends in resistance observed from DC transport measurements, implying that the bulk carriers dominate the both DC transport and the optical conductivity.

We find that the frequency of the E_u^1 phonon changes dramatically between $0 \leqslant x \leqslant 1/3$ in our $Bi_2(Te_{(1-x)}Se_x)_3$ samples (as shown in figure 5a), in contrast to the A_g^1 Raman active mode, where the frequency does not significantly vary over this range of alloy fractions [9, 14, 16]. This highlights the key role that the C_2 site (in the centre of the quintuple layer structure) plays in the E_u^1 mode, and the preferential ordering of the $Bi_2(Te_{(1-x)}Se_x)_3$ alloy.

We note that the change in crystalline anharmonicity, caused by this preferential order is key to understanding the temperature dependence of the vibrational properties of $Bi_2(Te_{(1-x)}Se_x)_3$; as the Se fraction, x, approaches 1/3, we find that the red shift of the E_u^1 phonon is smallest because the preferential ordering will warp the quintuple layer away from a rock salt-like structure, disrupting the long-range crystalline interactions that are displayed in Bi_2Te_3 [18]. However, as x increases past 1/3, C_1 sites on the outside of the quintuple layer start being partially occupied with Se, re-forming the rock salt-like crystal structure, and re-establishing these long-range interactions, thus increasing the rate at which the phonon red-shifts on cooling.

We also find that the E_u^1 phonon appears to couple to an electronic continuum at low temperature, indicated by an increase in the phonon linewidth and a change in the resonant frequency of the phonon mode. Similar effects have been seen in the Raman active modes of Bi_2Se_3 and Bi_2Te_3 [17], which have been attributed to the coupling between the phonon mode and the surface states. However, in our samples we observe this coupling in samples where the transport, and by extension the optical conductivity, is dominated by bulk carriers. These results support the prediction that the E_u^1 mode should couple strongly to the surface states within these topological insulators [8]. However it is important to note that coupling to bulk states, such as impurity bands, cannot be ruled out without further measurements.

V. ACKNOWLEDGEMENTS

ADB would like to thank John Kendrick for useful discussions and their theoretical insight. This work was supported financially by the Engineering and Physical Sciences Research Council (EPSRC) through the grants 'NAME' (EP/V001914/1) and 'HyperTerahertz' (EP/P021859/1), as well as by the European Union through the project 'EXTREME-IR' (EU Project No. 964735). The samples were grown in the Royce Deposition system at the University of Leeds, which is supported by the Henry Royce Institute, UK, through the EPSRC grants EP/P022464/1 and EP/R00661X/1. ADB also acknowledges funding from the EPSRC (EP/P007449/1).

---

[1] C. L. Kane and E. J. Mele, Quantum spin hall effect in graphene, Phys Rev Lett **95**, 226801 (2005).

[2] C. Chen, Z. Xie, Y. Feng, H. Yi, A. Liang, S. He, D. Mou, J. He, Y. Peng, X. Liu, Y. Liu, L. Zhao, G. Liu, X. Dong, J. Zhang, L. Yu, X. Wang, Q. Peng, Z. Wang, S. Zhang, F. Yang, C. Chen, Z. Xu, and X. J. Zhou, Tunable dirac fermion dynamics in topological insulators, Scientific Reports 2013 3:1 **3**, 1 (2013).

[3] X. H. Zhang, L. Q. Yu, S. von Molnar, Z. Fisk, and P. Xiong, Nonlinear hall effect as a signature of electronic phase separation in the semimetallic ferromagnet EuB_6, Phys Rev Lett **103**, 106602 (2009).

[4] Y. Wang, B. Qiu, A. J. McGaughey, X. Ruan, and X. Xu, Mode-wise thermal conductivity of bismuth telluride, Journal of Heat Transfer **135** (2013).

[5] B. Huang, P. Zhai, X. Yang, and G. Li, Effects of mass fluctuation on thermal transport properties in bulk Bi_2Te_3, Journal of Electronic Materials **46**, 2797 (2017).

[6] T. Stauber, G. Gómez-Santos, and L. Brey, Plasmonics in topological insulators: Spin–charge separation, the influence of the inversion layer, and phonon–plasmon coupling, ACS Photonics **4**, 2978 (2017).

[7] T. Hakioğlu, Effect of the electron-phonon interaction on the spin texture in $Bi_{2-y}Sb_ySe_{3-x}Te_x$, Physical Review B **100**, 165407 (2019).

[8] R. Heid, I. Y. Sklyadneva, and E. V. Chulkov, Electron-phonon coupling in topological surface states: The role of polar optical modes, Scientific Reports **7** (2017).

[9] W. Richter and C. R. Becker, A raman and far-infrared investigation of phonons in the rhombohedral V_2–VI_3 compounds Bi_2Te_3, Bi_2Se_3, Sb_2Te_3 and $Bi_2(Te_{1-x}Se_x)_3$, $(Bi_{1-y}Sb_y)_2Te_3$, Physica Status Solidi (b) **84**, 619 (1977).

[10] A. Akrap, M. Tran, A. Ubaldini, J. Teyssier, E. Giannini, D. V. D. Marel, P. Lerch, and C. C. Homes, Optical properties of Bi_2Te_2Se at ambient and high pressures, Physical Review B - Condensed Matter and Materials Physics **86** (2012).

[11] P. D. Pietro, M. Ortolani, O. Limaj, A. D. Gaspare, V. Giliberti, F. Giorgianni, M. Brahlek, N. Bansal, N. Koirala, S. Oh, P. Calvani, and S. Lupi, Observation of dirac plasmons in a topological insulator, Nature Nanotechnology 2013 8:8 **8**, 556 (2013).

[12] P. Shekhar, S. Pendharker, D. Vick, M. Malac, and Z. Jacob, Fast electrons interacting with a natural hyperbolic medium: bismuth telluride, Optics Express, Vol. 27, Issue 5, pp. 6970-6975 **27**, 6970 (2019).

[13] J.-S. Wu, D. N. Basov, and M. M. Fogler, Topological insulators are tunable waveguides for hyperbolic polaritons, Physical Review B **92**, 205430 (2015).

[14] S. Schreyeck, K. Brunner, A. Kirchner, U. Bass, S. Grauer, C. Schumacher, C. Gould, G. Karczewski, J. Geurts, and L. W. Molenkamp, Kinetic limitation of chemical ordering in $Bi_2Te_{3-x}Se_x$ layers grown by molecular beam epitaxy, Journal of Physics: Condensed Matter **28**, 145002 (2016).

[15] J. R. Drabble and C. H. L. Goodman, Chemical bonding in bismuth telluride, Journal of Physics and Chemistry of Solids **5**, 142 (1958).

[16] Y. Tung, Y. F. Chiang, C. W. Chong, Z. X. Deng, Y. C. Chen, J. C. Huang, C. M. Cheng, T. W. Pi, K. D. Tsuei, Z. Li, and H. Qiu, Growth and characterization of molecular beam epitaxy-grown $Bi_2Te_{3-x}Se_x$ topological insulator alloys, Journal of Applied Physics **119** (2016).

[17] S. Buchenau, S. Scheitz, A. Sethi, J. E. Slimak, T. E. Glier, P. K. Das, T. Dankwort, L. Akinsinde, L. Kienle, A. Rusydi, C. Ulrich, S. L. Cooper, and M. Rübhausen, Temperature and magnetic field dependent raman study of electron-phonon interactions in thin films of Bi_2Se_3 and Bi_2Te_3 nanoflakes, Physical Review B **101**, 245431 (2020).

[18] S. Lee, K. Esfarjani, T. Luo, J. Zhou, Z. Tian, and G. Chen, Resonant bonding leads to low lattice thermal conductivity, Nature Communications 2014 5:1 **5**, 1 (2014).

[19] Z. Tian, K. Esfarjani, J. Shiomi, A. S. Henry, and G. Chen, On the importance of optical phonons to thermal conductivity in nanostructures, Applied Physics Letters **99**, 053122 (2011).

[20] N. Bansal, Y. S. Kim, E. Edrey, M. Brahlek, Y. Horibe, K. Iida, M. Tanimura, G. H. Li, T. Feng, H. D. Lee, T. Gustafsson, E. Andrei, and S. Oh, Epitaxial growth of topological insulator Bi_2Se_3 film on Si(111) with atomically sharp interface, Thin Solid Films **520**, 224 (2011).

[21] A. Fülöp, Y. Song, S. Charpentier, P. Shi, M. Ekström, L. Galletti, R. Arpaia, T. Bauch, F. Lombardi, and S. Wang, Phase transition of bismuth telluride thin films grown by mbe, Applied Physics Express **7**, 45503 (2014).

[22] D. R. Bacon, A. D. Burnett, M. Swithenbank, C. Russell, L. Li, C. D. Wood, J. Cunningham, E. H. Linfield, A. G. Davies, P. Dean, and J. R. Freeman, Free-space terahertz radiation from a LT-GaAs-on-quartz large-area photoconductive emitter, Optics Express **24**, 26986 (2016).

[23] K. L. Krewer, Z. Mics, J. Arabski, G. Schmerber, E. Beaurepaire, M. Bonn, and D. Turchinovich, Accurate terahertz spectroscopy of supported thin films by precise substrate thickness correction, Optics Letters, Vol. 43, Issue 3, pp. 447-450 **43**, 447 (2018).

[24] Y. Wang, T. P. Ginley, C. Zhang, and S. Law, Transport properties of $Bi_2(Se_{1-x}Te_x)_3$ thin films grown by molecular beam epitaxy, Journal of Vacuum Science and Technology B, Nanotechnology and Microelectronics: Materials, Processing, Measurement, and Phenomena **35**, 02B106 (2017).

[25] G. Wang, X. G. Zhu, Y. Y. Sun, Y. Y. Li, T. Zhang, J. Wen, X. Chen, K. He, L. L. Wang, X. C. Ma, J. F. Jia, S. B. Zhang, and Q. K. Xue, Topological insulator thin films of Bi_2Te_3 with controlled electronic structure, Advanced Materials **23**, 2929 (2011).

[26] T. Bathon, S. Achilli, P. Sessi, V. A. Golyashov, K. A. Kokh, O. E. Tereshchenko, and M. Bode, Experimental realization of a topological p-n junction by intrinsic defect grading, Advanced Materials **28**, 2183 (2016).

[27] M. A. Reed, W. P. Kirk, and P. S. Kobiela, Investigation of parallel conduction in $GaAs/Al_XGa_{1-X}As$ modulation-doped structures in the quantum limit, IEEE Journal of Quantum Electronics **22**, 1753 (1986).

[28] H. H. Wieder, Transport coefficients of InAs epilayers, Applied Physics Letters **25**, 206 (2003).

[29] N. P. Butch, K. Kirshenbaum, P. Syers, A. B. Sushkov, G. S. Jenkins, H. D. Drew, and J. Paglione, Strong surface scattering in ultrahigh-mobility Bi_2Se_3 topological insulator crystals, Physical Review B **81**, 241301 (2010).

[30] Y. Deshko, L. Krusin-Elbaum, V. Menon, A. Khanikaev, and J. Trevino, Surface plasmon polaritons in topological insulator nano-films and superlattices, Optics Express, Vol. 24, Issue 7, pp. 7398-7410 **24**, 7398 (2016).

[31] L. Wu, M. Brahlek, R. V. Aguilar, A. V. Stier, C. M. Morris, Y. Lubashevsky, L. S. Bilbro, N. Bansal, S. Oh, and N. P. Armitage, A sudden collapse in the transport lifetime across the topological phase transition in $(Bi_{1-x}In_x)_2Se_3$, Nature Physics 2013 9:7 **9**, 410 (2013).

[32] A. Khanikaev, J. Trevino, L. Krusin-Elbaum, V. Menon, and Y. Deshko, Surface plasmon polaritons in topological insulator nano-films and superlattices, Optics Express, Vol. 24, Issue 7, pp. 7398-7410 **24**, 7398 (2016).

[33] A. Soni, Z. Yanyuan, Y. Ligen, M. K. K. Aik, M. S. Dresselhaus, and Q. Xiong, Enhanced thermoelectric properties of solution grown $Bi_2Te_{3-x}Se_x$ nanoplatelet composites, Nano Letters **12**, 1203 (2012).

[34] J. Yuan, M. Zhao, W. Yu, Y. Lu, C. Chen, M. Xu, S. Li, K. Loh, and B. Qiaoliang, Raman spectroscopy of two-dimensional $Bi_2Te_xSe_{3-x}$ platelets produced by solvothermal method, Materials **8**, 5007 (2015).

[35] P. G. Huggard, J. A. Cluff, G. P. Moore, C. J. Shaw, S. R. Andrews, S. R. Keiding, E. H. Linfield, and D. A. Ritchie, Drude conductivity of highly doped GaAs at terahertz frequencies, Journal of Applied Physics **87**, 2382 (2000).

[36] S. Nashima, O. Morikawa, K. Takata, and M. Hangyo, Temperature dependence of optical and electronic properties of moderately doped silicon at terahertz frequencies, Journal of Applied Physics **90**, 837 (2001).

[37] N. A. Kabir, Y. Yoon, J. R. Knab, J. Y. Chen, A. G. Markelz, J. L. Reno, Y. Sadofyev, S. Johnson, Y. H. Zhang, and J. P. Bird, Terahertz transmission characteristics of high-mobility GaAs and InAs two-dimensional-electron-gas systems, Applied Physics Letters **89**, 132109 (2006).

[38] R. German, E. V. Komleva, P. Stein, V. G. Mazurenko, Z. Wang, S. V. Streltsov, Y. Ando, and P. H. M. V. Loosdrecht, Phonon mode calculations and raman spectroscopy of the bulk-insulating topological insulator $BiSbTeSe_2$, Physical Review Materials **3**, 54204 (2019).

[39] M. P. Deshpande, S. V. Bhatt, V. Sathe, R. Rao, and S. H. Chaki, Pressure and temperature dependence of raman spectra and their anharmonic effects in Bi_2Se_3 single crystal, Physica B: Condensed Matter **433**, 72 (2014).

[40] J. P. Heremans, R. J. Cava, and N. Samarth, Tetradymites as thermoelectrics and topological insulators, Nature Reviews Materials 2017 2:10 **2**, 1 (2017).

[41] M. Cardona and T. Ruf, Phonon self-energies in semiconductors: anharmonic and isotopic contributions, Solid State Communications **117**, 201 (2001).

[42] Y. Tian, S. Jia, R. J. Cava, R. Zhong, J. Schneeloch, G. Gu, and K. S. Burch, Understanding the evolution of anomalous anharmonicity in $Bi_2Te_{3-x}Se_x$, Physical Review B **95**, 094104 (2017).

[43] R. P. Lowndes, Anharmonicity in the silver and thallium halides: Far-infrared dielectric response, Phys. Rev. B **6**, 1490 (1972).

[44] J. Hafner, Ab-initio simulations of materials using VASP: Density-functional theory and beyond, Journal of Computational Chemistry **29**, 2044 (2008).

[45] J. P. Perdew, K. Burke, and M. Ernzerhof, Generalized gradient approximation made simple, Physical Review Letters **77**, 3865 (1996).

[46] S. Grimme, S. Ehrlich, and L. Goerigk, Effect of the damping function in dispersion corrected density functional theory, Journal of Computational Chemistry **32**, 1456 (2011).

[47] A. D. Becke and E. R. Johnson, A density-functional model of the dispersion interaction, The Journal of Chemical Physics **123**, 154101 (2005).

[48] P. E. Blöchl, Projector augmented-wave method, Physical Review B **50**, 17953 (1994).

[49] H. J. Monkhorst and J. D. Pack, Special points for brillouin-zone integrations, Phys. Rev. B **13**, 5188 (1976).

[50] A. Jain, S. P. Ong, G. Hautier, W. Chen, W. D. Richards, S. Dacek, S. Cholia, D. Gunter, D. Skinner, G. Ceder, and K. a. Persson, The materials project: A materials genome approach to accelerating materials innovation, APL Materials **1**, 11002 (2013).

[51] A. Togo and I. Tanaka, First principles phonon calculations in materials science, Scr. Mater. **108**, 1 (2015).

[52] J. M. Skelton, L. A. Burton, S. C. Parker, A. Walsh, C. E. Kim, A. Soon, J. Buckeridge, A. A. Sokol, C. R. A. Catlow, A. Togo, and I. Tanaka, Anharmonicity in the high-temperature Cmcm phase of SnSe: Soft modes and three-phonon interactions, Physical Review Letters

117, 075502 (2016).

[53] S. K. Mishra, S. Satpathy, and O. Jepsen, Electronic structure and thermoelectric properties of bismuth telluride and bismuth selenide, J. Phys.: Condens. Matter **9**, 461 (1997).

[54] J. A. Hagmann, X. Li, S. Chowdhury, S.-N. Dong, S. Rouvimov, S. J. Pookpanratana, K. M. Yu, T. A. Orlova, T. B. Bolin, C. U. Segre, D. G. Seiler, C. A. Richter, X. Liu, M. Dobrowolska, and J. K. Furdyna, Molecular beam epitaxy growth and structure of self-assembled Bi_2Se_3 /Bi_2 $MnSe_4$ multilayer heterostructures, New J. Phys **19**, 85002 (2017).

[55] B. Y. Decker, Y. X. Gan, and S. Calderon, Thermoelectric properties of bismuth telluride filled silicone, Journal of Thermal Engineering **1**, 402 (2015).

[56] P. Zhang, Y. Xue, and P. Dev, Electron–phonon renormalization and phonon anharmonicity in metals, Solid State Communications **148**, 151 (2008).

[57] E. G. Maksimov and S. V. Shulga, Nonadiabatic effects in optical phonon self-energy, Solid State Communications **97**, 553 (1996).

[58] G. S. Hegde, A. N. Prabhu, R. Y. Huang, and Y. K. Kuo, Reduction in thermal conductivity and electrical resistivity of indium and tellurium co-doped bismuth selenide thermoelectric system, Journal of Materials Science: Materials in Electronics 2020 31:22 **31**, 19511 (2020).

[59] M. Yao, C. Opeil, S. Wilson, and M. Zebarjadi, Experimental determination of phonon thermal conductivity and lorenz ratio of single-crystal bismuth telluride, MRS Communications **7**, 922 (2017).

[60] A. Shukla, M. Calandra, M. d'Astuto, M. Lazzeri, F. Mauri, C. Bellin, M. Krisch, J. Karpinski, S. M. Kazakov, J. Jun, D. Daghero, and K. Parlinski, Phonon dispersion and lifetimes in MgB_2, Physical Review Letters **90**, 95506 (2003).

[61] V. Wagner, G. Dolling, B. M. Powell, and G. Landwehr, Lattice vibrations of Bi_2Te_3, physica status solidi (b) **85**, 311 (1978).

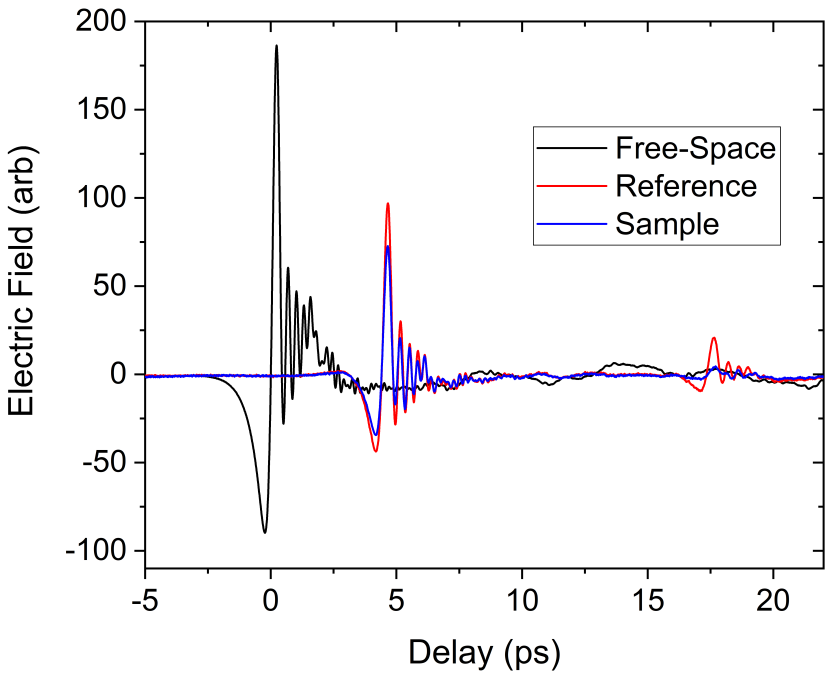

FIG. 1: Time-domain THz signal without a sample (black trace), the sapphire reference (red trace) and a 35 nm-thick Bi_2Te_3 film on an identical sapphire substrate (blue trace) at 290 K. The additional peak at 17.6 ps arises from Fabry-Perot reflections within the sapphire substrate.

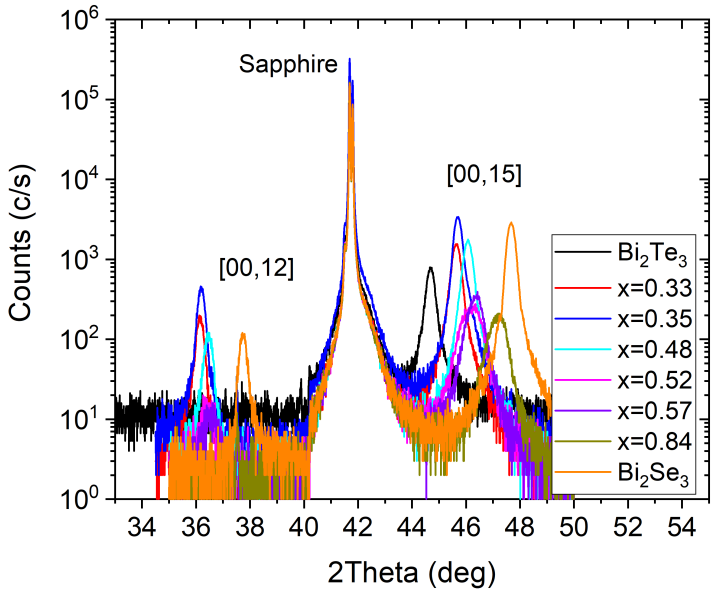

(a)

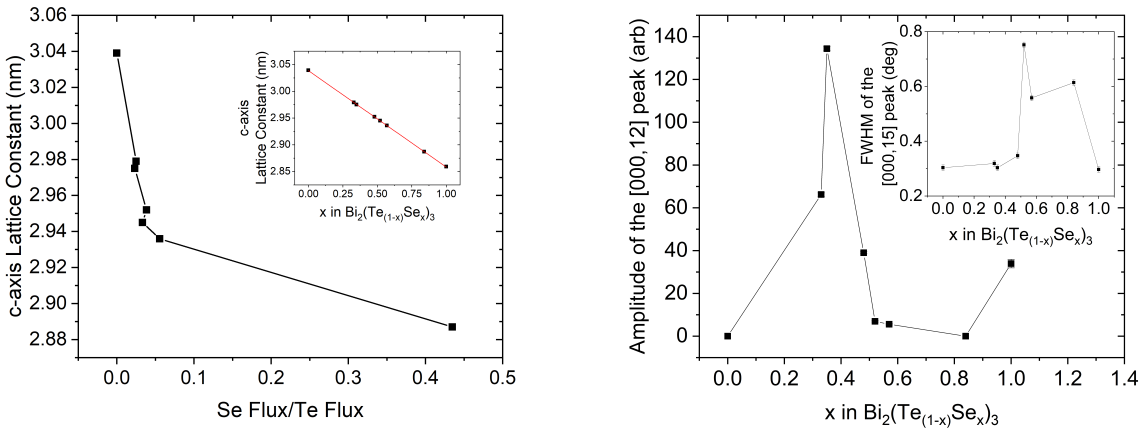

(b) (c)

FIG. 2: Structural characterisation of the samples involved in this study. a depicts the X-ray diffraction spectrum of the $Bi_2(Te_{(1-x)}Se_x)_3$samples, where the positions of the known diffraction peaks are labelled with the relevant miller indices. b shows the variation of the c-axis lattice parameter, calculated from the $[000, 15]$ peak, as the selenium flux is increased. The inset shows the Vegard's law analysis used to determine the nominal Se content. c shows the amplitude of the gaussian used to fit the [000,12] peak as a function of Se content. The inset shows the FWHM of the $[000, 15]$ peak, which is an indication of the large-scale disorder within the crystal.

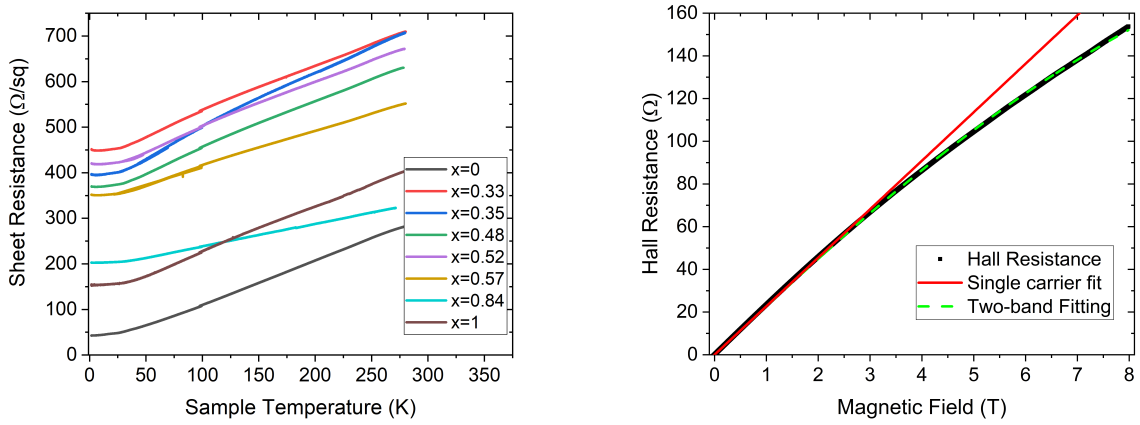

(a) (b)

FIG. 3: Summary of transport measurements performed on $Bi_2(Te_{(1-x)}Se_x)_3$ samples. a shows the variation in sheet resistance on cooling for the samples studied here. b shows the non-linearity in the Hall trace for the Bi_2Se_3 sample, with a linear fit to the low field ($B \leqslant 1$ T) shown in red, and a fit to the full two-band model shown in green.

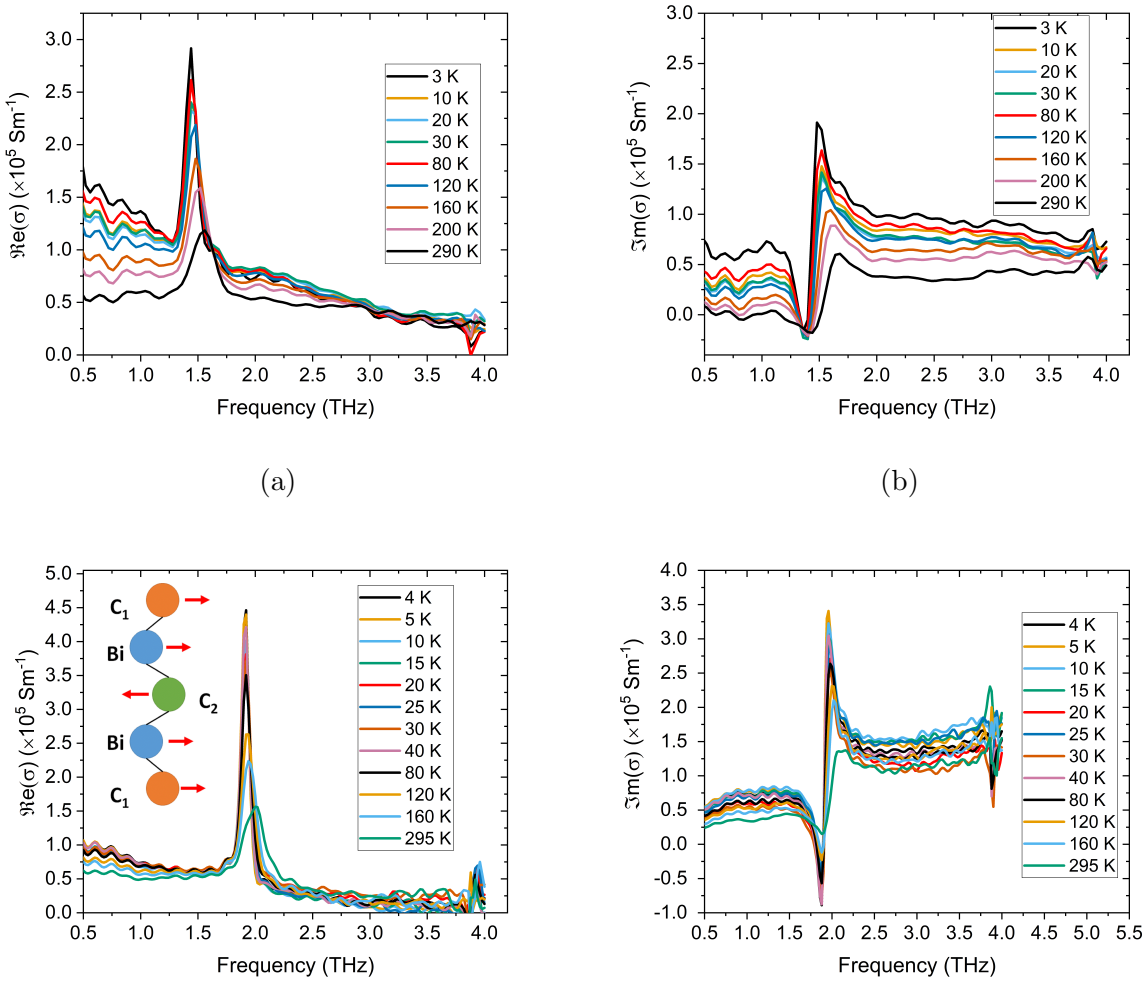

FIG. 4: Optical conductivities as a function of temperature of the binary topological insulator films, Bi_2Te_3 (a and b) and Bi_2Se_3 (c and d). a and c show the real part of the conductivities whereas b and d show the imaginary part of the conductivities. The resonance at ≈ 4 THz in all scans is an artefact of the quartz windows used here. The inset of c shows a schematic of the E_u^1 phonon mode responsible for the large resonance in the conductivity, where the black lines show the covalent bonds between atoms and the red arrows show the movement of the atoms that contribute to this phonon mode. Here, C represents sites that can be occupied by chalcogenides, Te or Se.

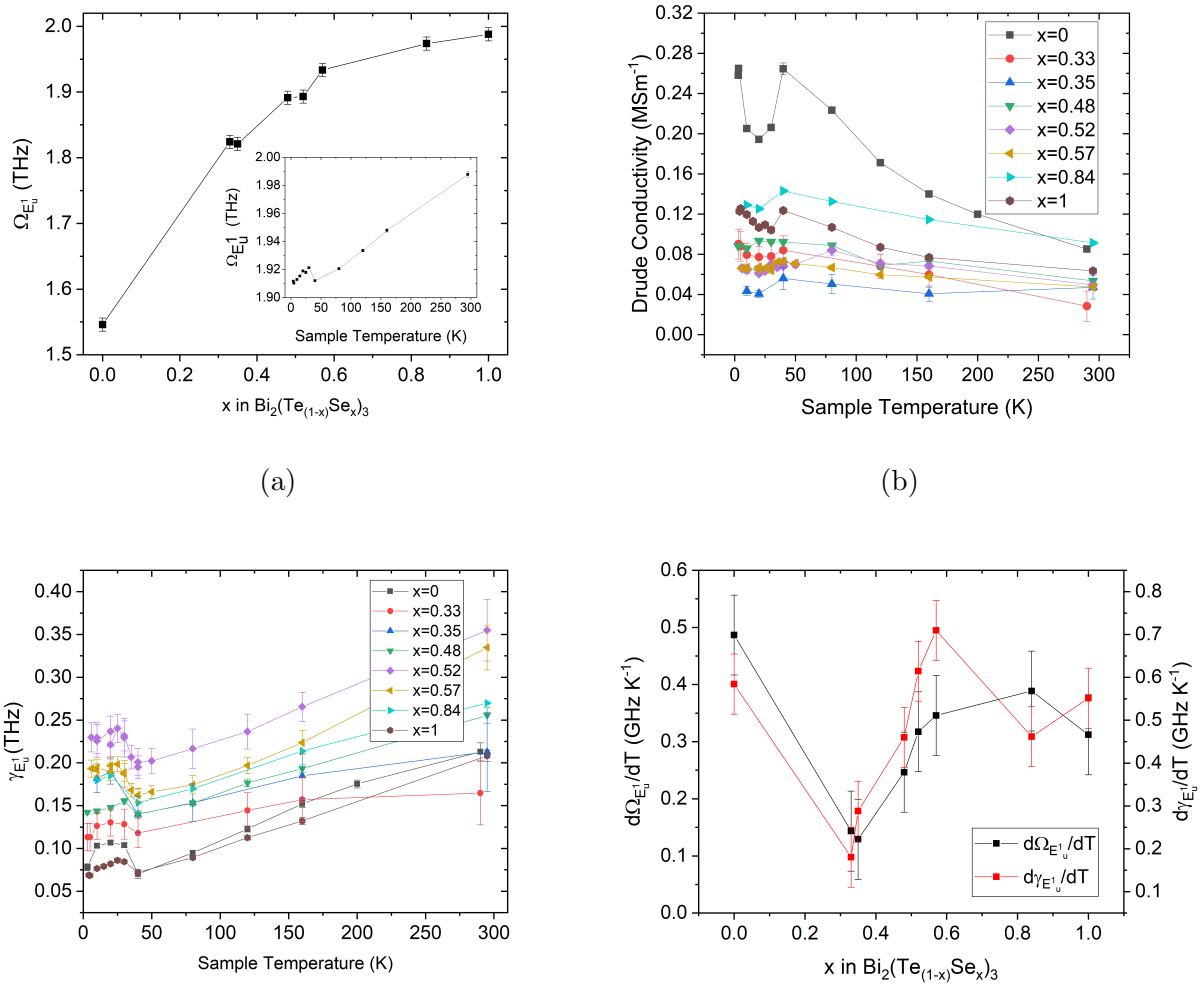

(a) (b)

(c) (d)

FIG. 5: Optical properties of the $Bi_2(Te_{(1-x)}Se_x)_3$ samples. a shows the variation of the phonon frequency at 290 K with Se content. The inset shows how the phonon frequency varies with temperature for the Bi_2Se_3 ($x = 1$) sample. b shows the DC conductivity, fitted from equation 2 as a function of alloy fraction and temperature. c shows the variation of the phonon scattering parameter $\gamma_{E_u^1}$ as a function of temperature for all the samples in this study, and d summarises the trends in the phonon frequency, $\Omega_{E_u^1}$, and phonon scattering parameter $\gamma_{E_u^1}$ in the high temperature regime (295 K$\geqslant$T$\geqslant$ 50 K).

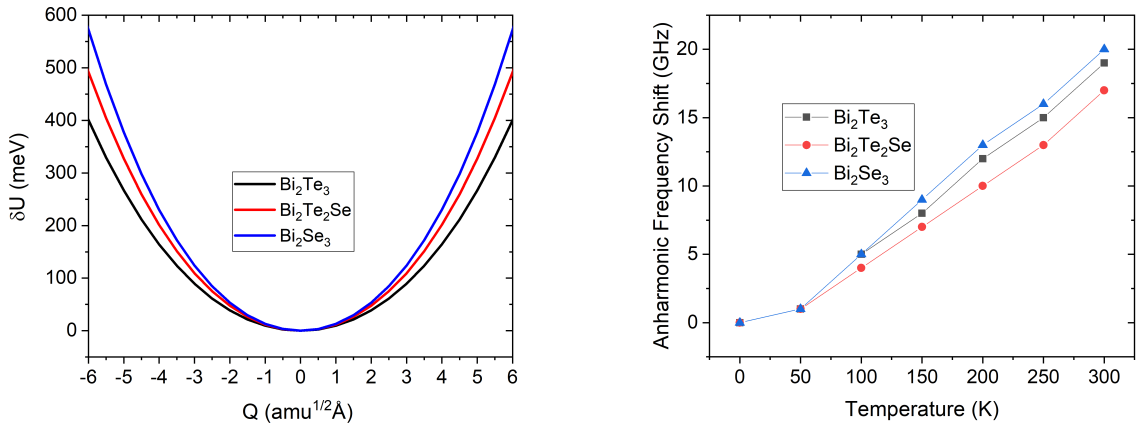

(a) (b)

FIG. 6: Summary of the density functional theory calculations performed on the E_u^1 modes within Bi_2Te_3, Bi_2Se_3 and Bi_2Te_2Se. a shows the potential energy surfaces for the phonon within Bi_2Te_3, Bi_2Se_3 and Bi_2Te_2Se, normalised around the phonon central frequency being at 0 energy. b shows the predicted anharmonic temperature dependent frequency shift for the Bi_2Te_3, Bi_2Se_3 and Bi_2Te_2Se.

TABLE I: Summary of the two-band Hall fitting for the $Bi_2(Te_{(1-x)}Se_x)_3$ samples studied here. All carrier densities were electron-like. The $x = 0.48$ and $x = 0.52$ samples did not show the non-linear Hall traces characteristic of two-carrier transport and so did not fit to the two-band model accurately.

x in $Bi_2(Te_{(1-x)}Se_x)_3$	Band 1 Carrier Density ($\times 10^{14}$ cm^{-2})	Band 1 Mobility ($cm^2V^{-1}s^{-1}$)	Band 2 Carrier Density ($\times 10^{12}$ cm^{-2})	Band 2 Mobility ($cm^2V^{-1}s^{-1}$)
0	1.2 ± 0.1	1100 ± 100	3.6 ± 0.3	5200 ± 500
0.33	0.75 ± 0.08	75 ± 7	26 ± 2	310 ± 30
0.35	1.8 ± 0.1	77 ± 7	15 ± 1	430 ± 40
0.48	0.79 ± 0.08	220 ± 20	-	-
0.52	0.83 ± 0.08	180 ± 20	-	-
0.57	1.3 ± 0.1	84 ± 8	17 ± 2	420 ± 40
0.84	1.3 ± 0.1	86 ± 8	29 ± 3	660 ± 70
1	0.65 ± 0.07	180 ± 20	14 ± 1	2000 ± 20